# A first-principles study of the effects of atom impurities, defects, strain, electric field and layer thickness on the electronic and magnetic properties of the C2N nanosheet

# Journal Pre-proof

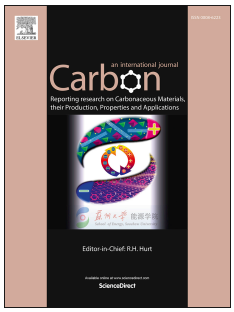


A first-principles study of the effects of atom impurities, defects, strain, electric field and layer thickness on the electronic and magnetic properties of the $C_2N$ nanosheet

Catherine Stampfl, A. Bafekry, Mitra Ghergherehchi, S. Farjami Shayesteh

PII: S0008-6223(19)31047-4

DOI: https://doi.org/10.1016/j.carbon.2019.10.038

Reference: CARBON 14700

To appear in: *Carbon*

Received Date: 6 July 2019

Revised Date: 15 October 2019

Accepted Date: 16 October 2019

Please cite this article as: C. Stampfl, A. Bafekry, M. Ghergherehchi, S. Farjami Shayesteh, A first-principles study of the effects of atom impurities, defects, strain, electric field and layer thickness on the electronic and magnetic properties of the $C_2N$ nanosheet, *Carbon* (2019), doi: https://doi.org/10.1016/j.carbon.2019.10.038.

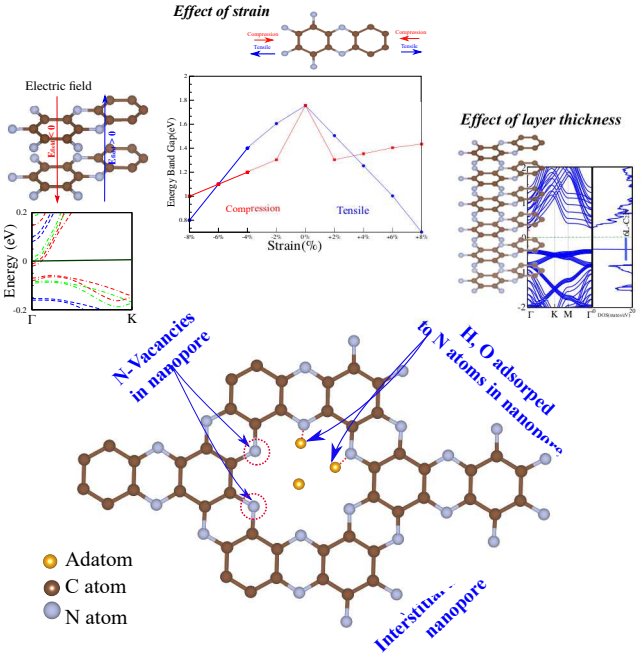

# A First-Principles Study of the effects of Atom Impurities, Defects, Strain, Electric Field and Layer Thickness on the Electronic and Magnetic Properties of the $C_2N$ nanosheet

A.Bafekry*,[1,2] Catherine Stampfl,[3] Mitra Ghergherehchi,[4] and S. Farjami Shayesteh[1]

[1] *Department of physics, University of Guilan, 41335-1914 Rasht, Iran*
[2] *Department of Physics, University of Antwerp, Groenenborgerlaan 171, B-2020 Antwerp, Belgium*
[3] *School of Physics, The University of Sydney, New South Wales 2006, Australia*
[4] *College of Electronic and Electrical Engineering, Sungkyun kwan University, Suwon, Korea*

Using the first-principles calculations, we explore the structural and novel electronic/optical properties of the $C_2N$ nanosheet. To this goal, we systematically investigate the affect of layer thickness, electrical field and strain on the electronic properties of the $C_2N$ nanosheet. By increasing the thickness of $C_2N$, we observed that the band gap decreases. Moreover, by applying an electrical field to bilayer $C_2N$, the band gap decreases and a semiconductor-to-metal transition can occur. Our results also confirm that uniaxial and biaxial strain can effectively alter the band gap of $C_2N$ monolayer. Furthermore, we show that the electronic and magnetic properties of $C_2N$ can be modified by the adsorption and substitution of various atoms. Depending on the species of embedded atoms, they may induce semiconductor (O, C, Si and Be), metal (S, N, P, Na, K, Mg and Ca), dilute-magnetic semiconductor (H, F, B), or ferro-magnetic-metal (Cl, Li) character in $C_2N$ monolayer. It was also found that the inclusion of hydrogen or oxygen impurities and nitrogen vacancies, can induce magnetism in the $C_2N$ monolayer. These extensive calculations can be useful to guide future studies to modify the electronic/optical properties of two-dimensional materials.

$C_2N$ nanosheet, Defect and strain engineering, Electronic structure, Electric field, Impurity of atom

## I. INTRODUCTION

Graphene,[1] as a two-dimensional (2D) layer crystal of carbon atoms, has attracted substantial interest and has been considered in a variety of potential applications in various fields.[2–10] Subsequently other 2D materials (2DM) including hexagonal boron-nitride (h-BN) and transition metal dichalcogenides have been extracted from layered bulk materials[11–13] and several monolayers from group IV elements, such as silicene, germanene, and stanene, have also been synthesized.[14–17] Also Mxene, a family of complex layered materials that are useful for various electrochemical energy storage devices.[18–20] The lack of a band gap is the major obstacle for the use of graphene in electronic applications, such as field-effect transistors, thus, opening of a band gap is of great technological importance.[21,22] Nitrogen doping has been widely studied as one of the most feasible methods to modulate the electronic and other properties of graphene and its derivatives.[23–25]

Recently, regarding the large subgroup of 2D crystals, intense attention has been paid to a special class of 2D conjugated polymers due to its anisotropic 2D geometric morphology, which can be stabilized as monolayers by taking advantage of the multifarious chemistry of carbon and nitrogen. The strong carbon bonds give rise to the unique properties of graphene, while these layered nanomaterials, composed solely of carbon and nitrogen atoms enable, nitrogen to take many different positions, which enhances the available possibilities to form strong covalent organic frameworks, resulting in remarkably high stiffness and strength in these nanomaterials.[26,27] These properties have enabled researchers to grow a number of so-called graphenic carbonitrides. $C_3N$ has been fabricated and was found to have interesting properties..[28–33,36,37] $C_3N_4$ exhibits semiconducting properties, with the possibility to be a potential photo-catalyst for water splitting.[38,39] Metal-free magnetism and half-metallicity in $C_4N_3$[40–42] was recently predicted theoretically to be useful in spintronic devices. $C_6N_6$ has been explored in experiments[43,44] and was investigated theoretically.[45] The successful synthesis and fabrication of $C_2N$, $C_3N$, $C_6N_8$, and $C_6N_6$ through bottom-up procedures motivated us to consider different approaches to tune the band gap.[46–48]

Nitrogenated holey graphene is one of the 2D carbon nitrite compounds with a stoichiometric formula of $C_2N$, that contains an evenly distributed lattice of N and hole sites which has been fabricated[49] and found to have excellent optical, thermal, mechanical, electronic, and magnetic properties.[50] Generally, the use of point defects, including vacancies, impurities, and interstitial atoms are an efficient approach to modify the electronic properties and of fundamental importance in 2DM, which can be used to effectively modify the intrinsic characteristics, and consequently used for a wide range of applications. Several approaches have been developed to modify the electronic and magnetic properties of $C_2N$ and other two-dimensional materials. These methods include the adsorption and substitution of atoms,[51–55] surface functionalizing with atom and molecule,[56–61] defect engineering,[62–64] applying electric field,[65,66] strain,[67,68] and edge states.[65,69,70] Generally, the substitution of atoms into a 2DM is of fundamental importance, as doing so enables a wide range of application devices by tailoring the electronic and magnetic properties, which is

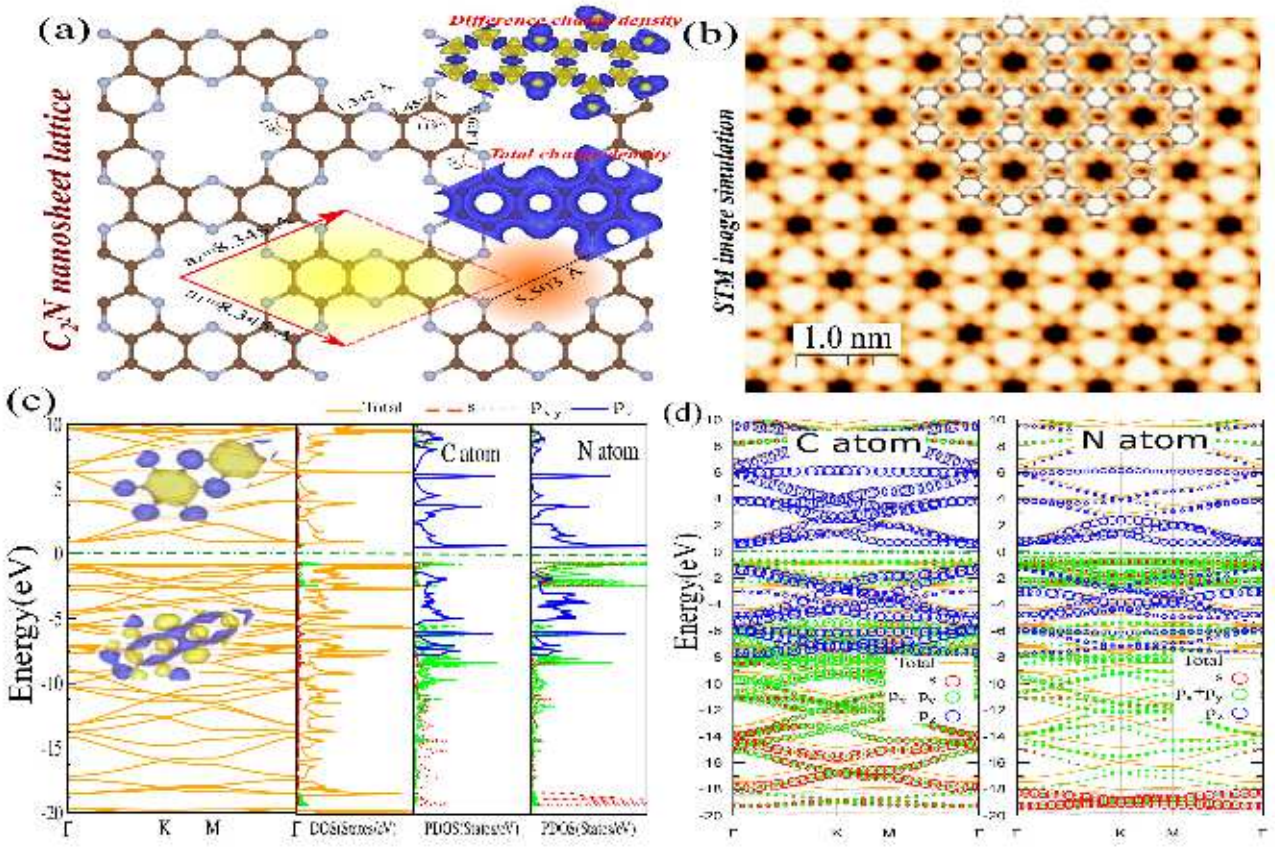


Figure 1. (a) Geometrical atomic structure of $C_2N$, with its hexagonal primitive unit cell indicated by the red parallelogram. The gray (blue) balls are C (N) atoms. The total (bottom) and difference (up) charge density are also shown in the same panel. (b) Simulated STM image of $C_2N$ over layered with the $C_2N$ lattice. (c) Electronic structure, DOS and PDOS. Charge densities of VBM and CBM are indicated as inset. The blue and yellow regions represent charge accumulation and depletion, respectively. (d) Orbital-resolved electronic band structure. The zero energy is set to the Fermi level energy ($E_F$).

useful for numerous applications such as photo-catalyst applications[71–74]

In this paper, after investigating the structural, electronic and optical properties of pristine monolayer $C_2N$, we aim to study the effect of the number of layers of $C_2N$ nanosheets, application of an electric field for bilayer $C_2N$, and strain for single layer $C_2N$, in order to determine if the character of $C_2N$ is altered, e.g. if it becomes metallic, half-metallic, a spin glass-semiconductor, a dilute-magnetic semiconductor. Moreover, we consider the inclusion of hydrogen and oxygen atoms, as well as nitrogen atom vacancies in the holey site of the $C_2N$ nanosheet to learn if such functionalization is advantageous for the bandstructure engineering of this novel 2D material.

## II. METHODS

In this paper, we performed calculations of the electronic structure with geometric optimization, using spin-polarized density functional theory (DFT) as implemented in OpenMX Package..[75] This code self-consistently finds the eigenvalues and eigenfunctions of the Kohn-Sham equations for the systems under study using norm-conserving pseudopotentials,[76] and pseudoatomic orbitals (PAOs).[77,78] In addition, we used the Perdew-Burke-Ernzerhof generalized gradient approximation (GGA) for the exchange and correlation.[79] Following the convergences tests, we chose a cutoff energy of 300 Ry for $C_2N$, so that the total energy converge below 1.0 meV/atom. The atomic positions were relaxed until the force convergence acting on each atom was under 1 meV/Å. The k-point mesh for sampling over the Brillouin zone (BZ) integration were generated using the Monkhorst-Pack.[80] For a primitive cell of hexagonal $C_2N$, a k-mesh of $21\times21\times1$ was used. The supercells were constructed with a 20 Å vacuum region normal to the $C_2N$ sheet so that interactions between $C_2N$ and its images are negligible. A $2\times2\times1$ supercell of $C_2N$, which contains 72 atoms, 48 C and 24 N atoms which in terms of x, y, z dimensions is defined as 16.69 Å, 16.69 Å, 20 Åis used for the studying lattice with N atom vacancies and those with adatom impurities. All systems are fully atomically relaxed in all directions. In order to accurately describe the vdW interaction, we adopted

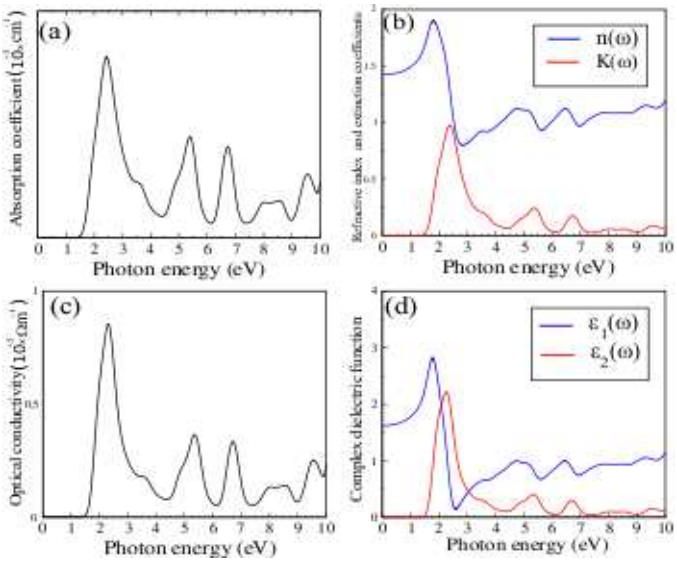


Figure 2. (a) Absorption coefficient, (b) refractive index, and extinction coefficient. (c) Optical conductivity and (d) real and imaginary parts of the complex dielectric function of monolayer $C_2N$.

the empirical correction method presented by Grimme (DFT-D2),[81] which has been proven reliable for describing long-range van der Waals (vdW) interactions. Simulated scanning tunneling microscopy (STM) images are obtained using the Tersoff-Hamann theory[82] for STM images, as supplied in the OpenMX code and presented using WSxM software.[83] We the computed the optical properties by using the SIESTA.[85] The exchange-correlation functional of the GGA-PBE is used. A 300 Ry mesh cut-off is chosen and self-consistent calculations are performed with a mixing rate of 0.1. Core electrons are replaced by norm-conserving, nonlocal Troullier-Martins pseudopotentials.[76] The convergence criterion for the density matrix is taken as $10^{-4}$ Ry.

## III. PRISTINE MONOLAYER $C_2N$

### A. Structural and electronic properties

From Fig. 1(a), we can see that $C_2N$ is composed of a hexagonal, 18-atom unit cell, consisting of 12 C and 6 N atoms (highlighted) and the primitive unit cell is indicated by a red parallelogram. The lattice constant of $C_2N$ is calculated to be 8.345 Å, which is in agreement with the experimentally obtained value of 8.3 Å[57] and previous theoretical calculations.[57,86–88] The calculated C-N bond length is 1.342 Å, while the, C-C bond lengths are 1.429 and 1.457 Å, respectively and the angle of C-N-C is 117°, slightly deviated from 120°. The holey site of $C_2N$, which forms a nanopore with a diameter of 5.503 Å (highlighted in orange), provides a reactive region inside for further functionalization by atoms or molecules. The total and difference charge density, are shown in Fig. 1(a), electron in such a way that the blue and yellow regions represent charge accumulation and depletion, respectively. The total charge density shows a high charge density around the N atoms, projecting toward the C-N bonds, indicating charge transfer from C to N atoms. In this way the C-N bonds achieve a partially covalent bond character. In order to provide visible guidance for experimental observations, are also calculate the STM image which is shown in Fig. 1(b). To correlate the STM image with the corresponding atomistic structure, we overlayered it with the $C_2N$ structure with the C (gray ball) and the N (blue ball) atoms. From the predicted STM images of $C_2N$, it is easy to recognize and correlate them with the corresponding atomic structure. The region in the center of the hexagonal ring of C atoms exhibits the bright spots (see Fig. 1(b)), while the large pores correspond to the dark regions. Fig. 1(c) shows the electronic band structure, density of states (DOS), and partial DOS (PDOS) of $C_2N$. The charge densities of the valence band maximum (VBM) and conduction band minimum (CBM) is shown in the insets. We see that $C_2N$ is a direct semiconductor with a 1.75 eV band gap, with both the VBM and CBM located at the Γ point. The calculated band gap is in agreement with previous calculations.[63,89] From the DOS and PDOS, we find that the VBM is predominantly contributed by the N-$s, p_{x,y}$ orbitals, with a noticeable contribution from C-$p_{x,y}$, while the CBM is mainly composed of C/N-$p_z$ orbitals. In addition, we can see from the orbital-projected electronic band structure of $C_2N$ on C and N atoms, as presented in Fig. 1(d), that due to the pairing of $p_z$ orbital electrons of C and N atoms, the structure has a nonmagnetic ground state. Interestingly, there is a large DOS at the VBM, which could lead to transitions to different phases including magnetism, superconductivity, and other phenomena.

### B. Optical properties of monolayer $C_2N$

In the following we investigate the optical properties of monolayer $C_2N$, including the dielectric function, the absorption and extinction coefficient ($K(\omega)$), refractive index ($n(\omega)$), and conductivity using SIESTA. We find that the absorption coefficient is almost zero when the energy is below 1.35 eV, and for larger photon energies, the value of the absorption coefficient increases, which corresponds to the reported 1.75 eV direct band gap. We can observe many peaks within the energy range, and the structure of the peaks can be explained by inter-band transitions. The absorption spectrum starts at about 1.55 eV, after which the intensity varies with increase in photon energy, reaching a maximum value of $24.06\times10^4$ at 2.44 eV. The major peak appears in a broad energy range of 2.0-3.0 eV, which indicates the pronounced absorption of visible light (see Fig. 2(a)). The other absorption peaks are located at 5.40 eV and 6.73 eV (in the ultraviolet region). The coefficients of $n(\omega)$ and $K(\omega)$, are shown in Fig. 2(b). Our result show that the static refractive index is $n(0)$= 1.41, while the maximum refractive index is 1.81

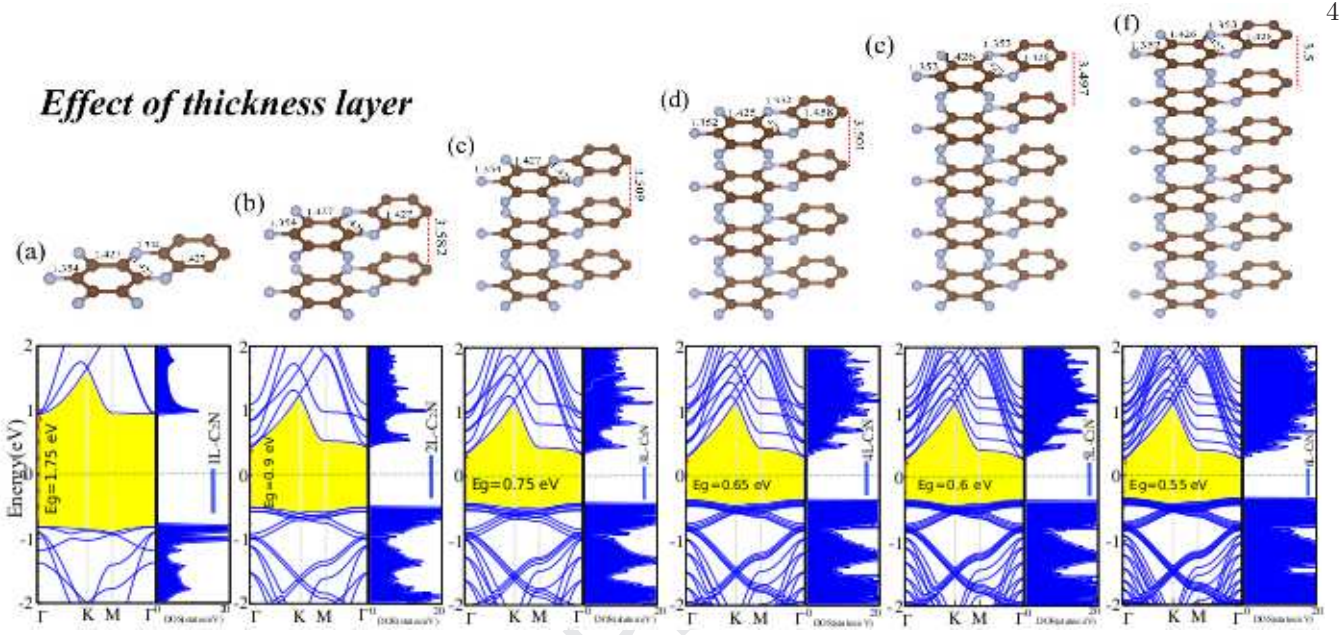


Figure 3. Optimized structures (upper panel) and band structure with corresponding DOS (lower panel) for different layer thickness of $C_2N$ (a) 1L, (b) 2L, (c) 3L, (d) 4L, (e) 5L and (f) 6L. The zero of energy is set to $E_F$, as shown by the dashed green-point line. Structural parameters including bond lengths and interlayer distance are shown in the same panel.

at 1.91 eV. We can see that at high photon energy, the refractive index eventually tends to one. The maximum of $K(\omega)$ is located at 2.40 eV and the spectrum curve of the refractive index and extinction coefficient rapidly decrease with increasing photon energy in the UV region. The optical conductivity is shown in Fig. 2(c). We found that the peak absorption happens at the photon energy of 2.30 eV, and gradually reduces to zero in the high energy region. The real and imaginary parts of the complex dielectric function, are shown in Fig. 2(d). In addition, the static dielectric constant in the zero frequency limit is obtained as $\varepsilon_1(0)$=2.02. We observe no negative values in the real part of the dielectric function, resulting in $C_2N$ exhibiting semiconductor character in this frequency region. Moreover, in the imaginary part of the dielectric function $\varepsilon_2(\omega)$, there is mainly one peak, which has a value of 2.78 at 2.27 eV.

## IV. EFFECTS OF LAYER THICKNESS, ELECTRIC FIELD AND STRAIN

We constructed a few layers of $C_2N$ with the stacking sequence of AA. In the AA stacking, the in-plane positions of the atoms on the layers are exactly the same. In the following, the monolayer to hexalayer of $C_2N$ is labeled by 1L- to 6L-$C_2N$. The optimized atomic structures from monolayer to hexalayer of $C_2N$ are shown in Figs. 3(a-f), respectively. Following the geometry optimization and energy minimization, the interlayer distances between the layers of $C_2N$ in the sandwich structures are determined to be 3.509 Å. We can see that there is no buckling in the structure of a few layers after optimization. The inter-layer distances between the layers of $C_2N$ are obtained range from 3.463 to 3.582 Å and the in-plane covalent bond lengths are about 1.398 Å (C-C atoms) and 1.408 Å (C-N atoms). These values can be compared to those of $C_2N$ which are 1.403 and 1.404 Å, respectively. It is interesting to investigate the effect of layer number on the electronic properties of nL-$C_2N$ by calculating the band structure and DOS, which are shown in Fig. 3. Our results show that with increase of number layer of $C_2N$, the electronic states is modified. In particular, the band gap of $C_2N$ varies depending on the number of layers and decreases from 1.75 eV for 1L-$C_2N$ to 0.55 eV for 6L-$C_2N$. Due to the tunable of band gap over a wide range, few layer $C_2N$ materials may have tremendous opportunity for application in nanoscale electronic and optoelectronic devices.

Application of an external electric field can significantly alter the position of electronic states. Here, we investigate the effect of an external, uniform electric field on the electronic properties of bilayer $C_2N$. The electronic structure of bilayer $C_2N$ under application of a perpendicular electric field, are shown in Figs. 4 (a,b). The strength of electric field (F) is varied from -0.8 to +0.8 V/Å, and F>0 and F<0 denotes parallel and anti-parallel to the z-axis, respectively. We can see that the band gap decreases and a semiconductor-to-metal transition occurs. As a result, it is possible to tune the electronic properties and control the Fermi-level by using an electric field. We can see that, when applying an electric field on bilayer $C_2N$, its band gap will decrease and a semiconductor-to-metal transition occurs. As a result, it is possible to tune the electronic properties and control the Fermi-level by using an electric field.

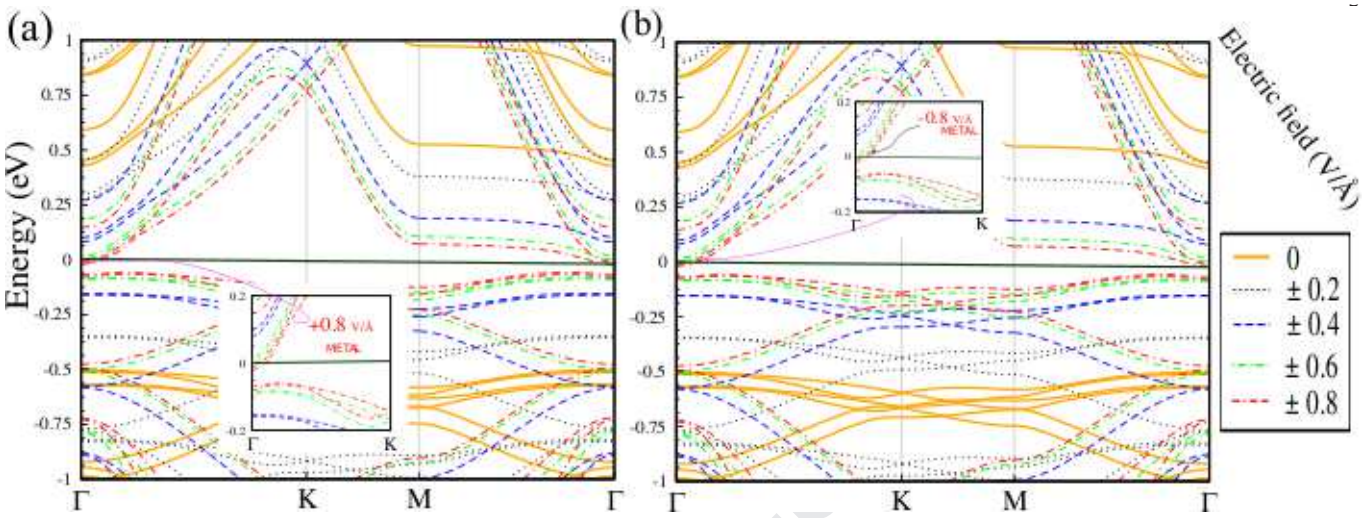


Figure 4. Electronic structure of bilayer $C_2N$ under an electric field in the normal direction. The perpendicular electric field >0 and <0 that denotes parallel and antiparallel to the z-axis, respectively. The zero of energy is set at $E_F$ indicated by horizontal line.

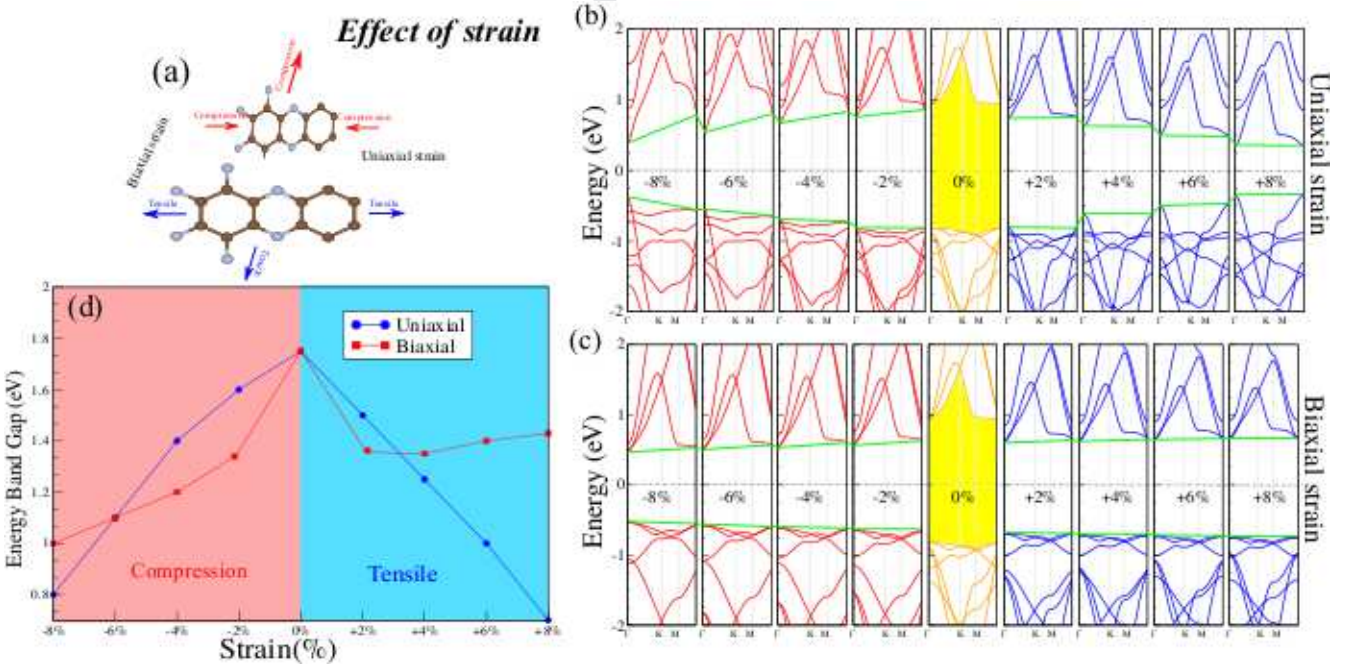


Figure 5. (a) Schematic model of strain applied on monolayer $C_2N$ along x-y axis. Electronic band structure as a function of (b) uniaxial strain and (c) biaxial strain. The zero of energy is set at $E_F$ as shown by the dashed green-point line. (d) Energy band gap as a function of uniaxial and biaxial strain.

In the following, we investigate the effects of uniaxial and biaxial strain (tensile and compression states) on monolayer $C_2N$. The tensile and compression strains are defined as $\varepsilon = (a - a_0)/a_0 \times 100$, where $a$ and $a_0$ are the strained and non-strained lattice constants. The uniaxial and biaxial strain is applied along a-axis (zigzag direction) and a-b axis, respectively. Schematic view of the atomic structure and applied strain directions and, electronic structure of monolayer $C_2N$ under uniaxial and biaxial strains, are shown in Figs. 5(a-c). We find that the band gap decreases with increasing uniaxial strain and can become metal when it exceeds -8 %. By contrast, in the case of biaxial tensile strain, semiconducting behavior is found for strain up to +8 %, while for the biaxial compression, with increasing strain, the band gap decreases. The energy band gap as a function of uniaxial and biaxial strain are shown in Fig. 5(d). Our result show that the band gap is increased from 0.4 eV as biaxial tensile strain and the band gap, with increasing biaxial compression strain becomes metal at -8 %.

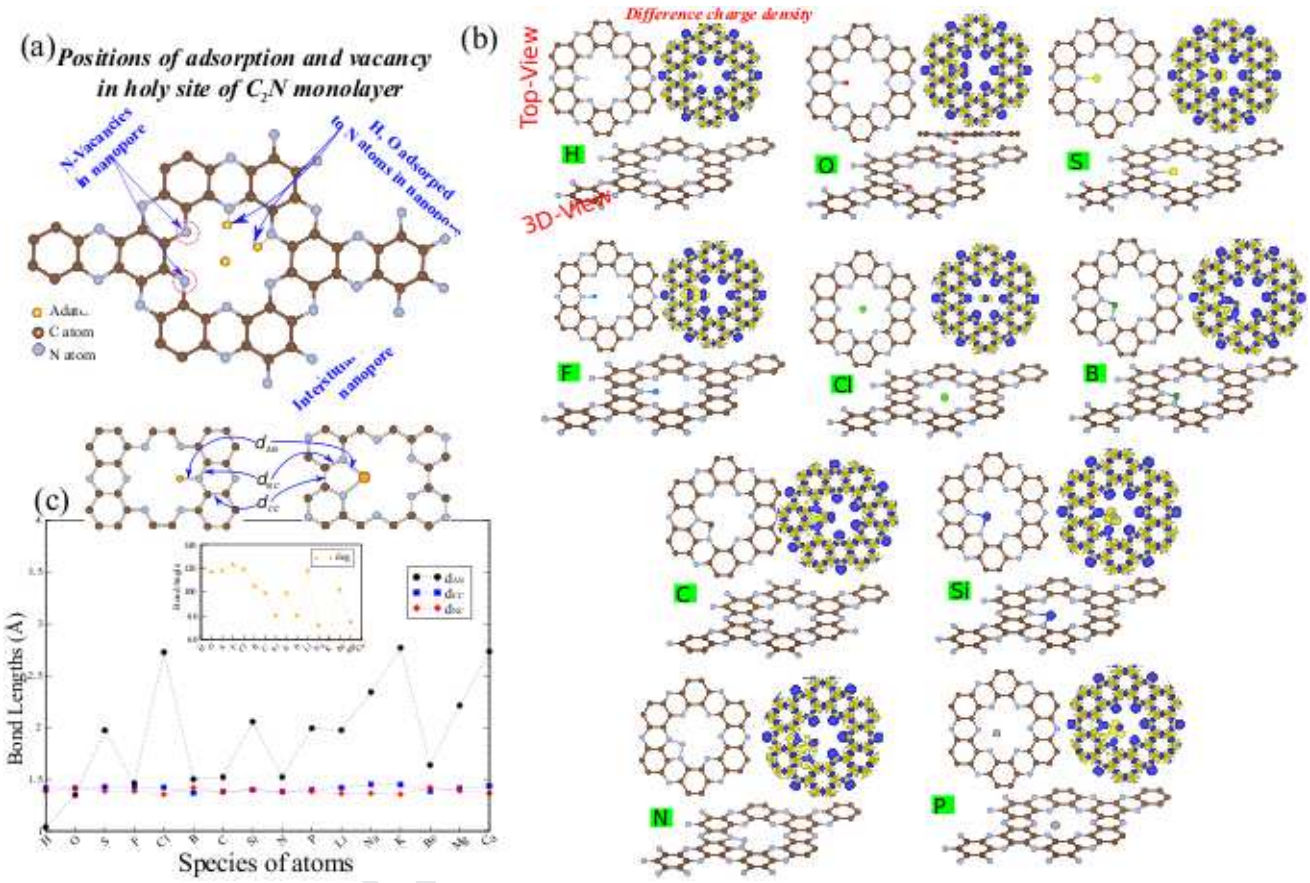


Figure 6. (a) Schematic view of geometric structures for the position of hydrogen and oxygen atoms impurities, interstitial atoms and N-vacancies in holey site of $C_2N$. (b) Top and prospective views of the optimized atomic structures for different atoms. Difference charge densities are shown in the same panel. The blue and yellow regions represent the charge accumulation and depletion, respectively. (c) Structural parameters including bond length, bond angels. The atomic structure is also given in the same panel.

We now study the effects of defects including adatom adsorption and nitrogen vacancies into holey site of monolayer $C_2N$. A $2 \times 2 \times 1$ super-cell consisting of 72 atom, was tested as to determine whether it was sufficiently large for the simulation of defects. The schematic view of the structures, regarding position of adsorbed interstitial atoms and N-vacancies in the holey site of $C_2N$ are shown in Fig. 6(a). The optimized atomic structures of H, O, S, F ,Cl, B, C, Si, N, and P atom impurities are shown in Fig. 6(b). These atoms are located in the center of the $C_2N$ nanopore and form a single or two covalent bond between N and atom. These is a slight a local distortion in the atomic structures around the atom. The H, O, S, and F atoms interact through $sp^2$-hybridization and form single covalent $\sigma$ bonds with neighboring N atoms. It can be see from Fig. 6(b) that the N atom bonded to the impurity undergoes a notable shift towards the adatom, thus the N-C and C-C bond lengths are elongated in comparison with the N-C (1.349 Å) and C-C (1.421 Å) bond lengths in pristine $C_2N$. Following relaxation, the distance, $d_{AN}$, between the adatom and its nearest N atom, ranges from 1.038 Å (for H) to 1.462 Å (for F), and most of them occur around 1.4 Å. The C-N-C bond angles are in the range of 117-123°. The variation of structural parameters including the bond lengths and bond angles for various atoms adsorbed on $C_2N$ are schematically shown in Fig. 6(c). In addition, B, C, Si, N, and P adatoms, interact through $sp^2$-hybridization and form two covalent bonds with nearest N atoms, and as a result, the N atoms shifts towards adatoms. In order to better understand the bond character, the difference charge density of Ad/$C_2N$ systems, is shown in Fig. 6(b). Note, that there is a charge accumulation in the region between adatom and neighboring N atom, which results in a strong Ad-N covalent bond. The structural parameters including $d_{AC}$, $d_{CC}$, $d_{NC}$, are shown in Figs. 6(c). We can see that the $d_{CC}$ and $d_{NC}$ are elongated $\sim$ 1.4 Å and $d_{AC}$ are very short between 1.5-2.1 Å. Incidentally, adsorption of an O atom induces a buckling in the range of 0.4 Å, with a covalent bond character, while there is no such buckling for other species of atoms.

We now investigate how the electronic and magnetic properties of $C_2N$ are modified by adsorption of the impurities, by calculating the band structure, DOS and PDOS (Fig. 7(a). The energy bands closely below and above the Fermi energy, are mainly attributable to the

adatom states and appear as localized impurity states. We can see that the interaction of these atoms with $C_2N$ induces a range of electronic character, including metal, semiconductor and spin-glass semiconductor. The S,Cl/$C_2N$ system, becomes a metal and the O/$C_2N$ is a direct semiconductor with a 1.2 eV band gap. Interestingly, we can see that the H and F/$C_2N$ systems, are a dilute-magnetic semiconductor with a 1.1 and 1 eV band gap in both the ↑ and ↓ spin channels and have a 1 $\mu_B$ magnetic moment. The dilute-magnetic semiconductors could lead to many new prospects for practical applications, such as spin photo-diodes, spin detectors and electromagnetic radiation generators for over a variety range of wavelengths based on spin photo-conductivity. These atoms mostly provide a p-type charge carrier by moving the $E_F$ to the VB edge. The Cl/$C_2N$ system exhibits a ferromagnetic-metal with a magnetic moment of 1 $\mu_B$.

It can be seen from the DOS and PDOS shown in Fig. 7(b) that the VBM of the Ad/$C_2N$ systems is due to the hybridization of $s$ and $p_z$ states of the atoms and the $p_z$ orbitals of the nearest C or N atoms. In comparison with $C_2N$, the band structure is substantially changed due to the strong disturbance of $p_z$ states caused by the adatoms. This illustrates that the interaction between the adatom and $C_2N$ may be determined by adatom $p_z$-orbital states as opposed to $s$-orbital states. For the S/$C_2N$ system the main contributions of the VBM and CBM come from S-$p_z$ and C/N-$p_z$ orbital hybridization, whereas the S-$p_{x,y}$ orbital does not mix with C and N states. The C and Si/$C_2N$ systems become direct semiconductors with a band-gap of 0.8 and 1.1 eV, respectively. The Si/$C_2N$ system shows a dilute-magnetic semiconductor behavior and has a 1 $\mu_B$ magnetic moment, while the band gap in the ↑ and ↓ spin states is 1 eV. The interaction of N and P atoms with $C_2N$ eliminates the semiconducting band gap and induces metallic properties. These atoms mostly provide a p-type charge carrier. The ground state of $C_2N$ is nonmagnetic and the C, Si, N and P/$C_2N$ systems exhibit a nonmagnetic ground state, except for B in which magnetic moment is 1 $\mu_B$.

Next, we study the adsorption of Li, Na, K, Be, Mg, Ca and Al atoms on $C_2N$. The optimized structure and structural parameters including atomic bond length and bond angles are shown in Fig. S1. The band structure, DOS and PDOS of Ad/$C_2N$ systems (Ad= Li, Na, K, Be, Mg and Ca) is shown in Fig. 8(a). We find that depending on the atomic species, the semiconducting nature of the energy band structure of $C_2N$ is either eliminated or preserved. Compared to the band structure of $C_2N$, it can be seen that the adatom energy bands are mainly concentrated near $E_F$. The main dispersion bands of $C_2N$ are maintained on adsorption of these atoms, indicating that the bonding is ionic nature, as consistent with the density difference distributions. Adsorption of the Li adatom can induces a magnetic moment of 0.43 $\mu_B$ in $C_2N$. For the other alkali metals, we find that the Na, K, Mg and Ca adatoms systems exhibit metallic characteristic, with the impurity states appearing near the VBM and CBM edges. For the Be adatom system, it is a direct semiconductor with a 1.1 eV band gap, with the VBM and CBM located at the Γ point, and no significant changes are found near the VB and CB edges. In Fig. 8(b), the DOS and PDOS are shown for the Li, Na, K, Be, Mg, and Ca adatom systems. Based on the calculated DOS and PDOS, we find both the CBM and VBM receive contributions mainly from hybridization of the adatoms-$p_z$ and C/N-$p_z$ orbitals.

## V. EFFECT OF CONCENTRATION OF H, O ATOMS AND N-VACANCIES

In the following we systematically investigate the structural and electronic properties of $C_2N$ with H and O atoms impurities adsorbed for different coverages, in the holey site of monolayer $C_2N$. This structures induce metallic character, which can be continuously tuned by varying the hydrogen and oxygen coverage from 3.1 to 12.5 % (six homogeneous coverages. The planar C-N lattice of adsorbed perfect monolayer $C_2N$ is constructed of rings composed of carbon and nitrogen atoms, which surround the large holes within the holey structure. The planar structure can be well maintained in the presence of defects such as the N vacancy or substitutional impurities, while impurity atoms, they generally are not in the same plane as the $C_2N$ lattice. We can clearly see that adsorption of hydrogen and oxygen impurities, modifies the atomic structure compared to the pristine $C_2N$ (see Figs. 9(a,b)). In addition for thw adsorption of the H atom into holey site a planar structure with one N atom passivated by the H atom. In the case of 1H/$C_2N$ (3.1%), the nearest N atom to H moves in the upward direction and when the H coverage increases to two (2.77%), the surface distortion becomes more apparent and the bond length changes significantly. With further increase of H coverage, similar behavior is observed with a more distorted surface geometry (see Fig. 9(a)). For impurity O atoms, we find that the optimized lattice constant increases with coverage, due to the charge transfer from $C_2N$ to the O atoms (because of the large electro-negativity of the O atom) and the effect of the formation of epoxy groups at the C-N and C-C bonds. Considering the $C_2N$ with interstitial impurities, the O impurity into holey site should result in the C-O-C bridge bonds connecting the adjacent C atoms within the six-member C rings. After the O atom was added into the big hole ring, one of the edge N atoms will be saturated by the O atom and N-O bonds will not stay in the plane of C-N lattice. The $N_O$-O bond length is 1.34 Å, showing that the O atom is chemically adsorbed on $C_2N$ and the C-C and C-N bond lengths are elongated to 1.4 Å (see Fig. 9(b)).

The electronic band structure and corresponding DOS of H atoms impurities in $C_2N$, are shown in Figs. 10(a,b). Our results show that the electronic structure of $C_2N$ is significantly affected by H and O atom adsorption and exhibit diverse electronic and magnetic properties. The 1H and 3H/$C_2N$ system, exhibit a dilute-

magnetic semiconductor character, while the 5H/$C_2N$ shows ferromagnetic-metal behavior and induces a 1 $\mu_B$ magnetic moment. In contrast the 2H, 4H and 6H/$C_2N$ systems are a semiconductor with band gaps of 1, 0.95 and 0.8 eV, respectively, where the VBM and CBM are located at the Γ and K points. The 1O, 2O, and 6O/$C_2N$ systems, exhibit direct semiconductor character with band gaps of 1.2, 1, and 1.2 eV, respectively, while the VBM and CBM are at bothe the Γ point. We find that the 3O and 4O/$C_2N$ systems exhibit metallic character with no net spin. The DOS of these structures is different from that of $C_2N$, exhibiting an impurity state around $E_F$. For the 5O/$C_2N$ structure spin-splitting occurs in ↑ and ↓ spin channels and leads to ferromagnetic-metallic behavior with an induced magnetic moment of 1 $\mu_B$. It can be seen that the width of the band gap becomes narrow and decreases with the O/C ratio, reflecting the localization of the electronic states; that is, decreased charge transfer between C and N atoms in $C_2N$ with increase of epoxy groups. The difference charge density for the H and O impurity systems is shown in Fig. S2. There is a high charge density around the N and H atoms of $C_2N$. The high charge density around H atoms projecting toward the C-N and N-H bonds show a charge transfer from the N to H atom. In this way the C-N and N-H bonds achieve a covalent-like bonding. Recently, many methods, including defect engineering, were used to change the electronic properties of the 2D materials.[90? ? ,91] Here, we also investigate the effects of different N-vacancies at the holey site of $C_2N$ nanosheet. The optimized structures of the different concentration of N vacancies are shown in Figs. 11(a-f). We found that with the different N vacancies atomic reconstructions in the $C_2N$ nanosheet occur. It is relevant to note that in a previous study, authors concluded that the pristine and defective $C_2N$ nanosheet are thermally stable even at high temperatures.[50] The above-mentioned reconstructed geometries and redistributed electrons of $C_2N$ may lead to unique characteristics of these defective $C_2N$. The formation energies of defective $C_2N$ were also calculated to evaluate the relative stability and experimental feasibility of them. The band structure and DOS of $C_2N$ the with different N-vacancy concentrations are shown in Figs. 11(a-f). The electronic properties strongly depend on the N-vacancy configuration. In particular, the 3N- and 5N-vacancy structures exhibit a metallic character, while the 1N-, 2N-, 4N-, and 6N-vacancy structures become direct semiconductor with band gaps of 1.1, 1.3, 1.2 and 1 eV, respectively.

## VI. EFFECTS OF ATOM SUBSTITUTION

Due to the two-dimensionality of $C_2N$, the substitution of foreign atoms will affect the structural, electronic, and magnetic properties of pristine $C_2N$. We theoretically investigate the electronic structure of foreign atoms substituted in the lattice, namely H, O, S, F, Cl, B, C, Si, and P atoms with the N atom of monolayer $C_2N$. The optimized structures are shown in Fig. 12(a). We denote the substitution of atoms on the N site of $C_2N$ by $Sb_N$-$C_2N$. For example, when a H atom is substituted for a N atom of $C_2N$, it is labeled as $H_N - C_3N$. The variation of structural parameters, including lattice constant, atomic bond length and bond angles for the different species of atoms substituted on the N site are shown in Fig. 12(b). The schematic view of the substitution site is indicated in the same panel. The foreign atoms interact through $sp^2$-hybridization and form two $\sigma$ bonds with neighboring C atoms of $C_2N$. The bond lengths of the foreign atoms range from 1.34 to 1.54 Å, while the C-Sb-C bond angles are in the range of 119-135°. For foreign atoms with atomic radii larger than that of the N atom, such as S, F, Si and Cl, there is an expansion of lattice constant. The corresponding electronic band structures of $C_2N$ are shown in Fig. 13. The blue and red-dashed lines represent ↑ and ↓ spin states, respectively. The energy bands around the $E_F$ are mainly attributable to the foreign atom orbital states and appear as localized impurity states. We find that the interaction of foreign atoms with $C_2N$ can induce metallic and semiconducting properties. Both $O_N$ and $S_N$ systems, yield metallic behavior and no spin polarization. For the $H_N$, $F_N, Cl_N, B_N$ and $P_N$ systems, a semiconductor character is observed with direct band gaps of 1.6, 1.8, 1.6, 1.4, and 1.7 eV, respectively, where the VBM and CBM are located at the Γ point. The substitution of B and P atoms, transformed the system into a p-type semiconductor due to the tendency of these atoms to gain electrons, resulting in a down shift of the Fermi level inside the VBM edge thus exhibiting hole doping properties. The substitution of F and Cl systems have impurity states near the CBM edge, whereas no significant change is observed near the VBM edge. This suggests that $F_N$ and $Cl_N$ behaves as a donor atoms. Interestingly, the $C_N$ and $Si_N$ structures exhibit a dilute-magnetic semiconductor character, with band gaps of 1.7 and 1.1 eV, respectively. The VBM and CBM of $C_2N$ are influenced, leading to spin-splitting between the ↑ and ↓ spin channels. Because of the unpaired electron, the F atom attains a magnetic moment of 1$\mu_B$ in the ground state. From the PDOS in Fig. 13, we can see that the substitution of these atoms leads to more strongly delocalized VBM and CBM than pristine $C_2N$. The substituted structures also give rise to localized states in the fundamental band gap or resonance states in the VB and CBM of $C_2N$. From Fig. 13(a), it can also be seen for $O_N$ and $SN$ that the electronic states near the Fermi energy, $E_F$, are mainly governed by the C/N-$p_z$ with O and S-$p_z$ orbital states. For the $C_N$ and $Si_N$ systems, there is obviously asymmetry spin splitting around $E_F$ in the ↑ and ↓ spin channels, in result spin-polarized semiconductors (dilute-magnetic semiconductors) with a narrow, indirect band gap and the inducing of a magnetic moment in $C_2N$. For the system with $C_N$, the corresponding PDOS further reveal that these asymmetric impurity states in the band gap mainly come from the hybridization of C-$s$ with C-$p_{x,y}$ and N-$s$ orbital states in the ↑ spin channel inducing a magnetic moment of 1

$\mu_B$. However for the $Si_N$ structure, the hybridization is slightly different. For the $Si_N$ atom the Si-$p_z$ and C/N-$p_z$ orbital states and the CBM contribution come from Si-$s$ with C-$p_{x,y}$ orbitals in the $\downarrow$ spin channel. The VBM of the $P_N$ structure is attributed to the hybridization of P-$s$ and P-$p_{x,y}$ with C/N-$p_{x,y}$ orbitals states, and the CBM is due to the hybridization of P-$p_z$ with C/N-$p_{x,y}$ states.

## VII. MECHANICAL PROPERTIES

Finally, we study the mechanical stability of monolayer $C_2N$ under strain. We use a rectangular $2 \times 2$ supercell and consider uniaxial strain along the zigzag direction of +10% to +30%. From Fig. 14, clearly, we see that $C_2N$ can retain a stable structure under uniaxial strain with the value 10%, and its structure is completely deformed at 30%. Since the C-N bonds are stronger than the C-C bonds, first the C-C bonds are broken. These mechanical properties show that the $C_2N$ is highly mechanically stable and the high stability originates from strong bonding between C-C and C-N atoms.

## VIII. CONCLUSION

In summary, based on first-principles calculations, we explored the structural, electronic, and optical properties of the $C_2N$ nanosheet, which has been recently synthesized. We firstly investigated the electronic properties of few-layer $C_2N$ with different layer and we found the band gap decreases with increase in layer number. In addition, with applying an uniform electric field on the bilayer $C_2N$, the band gap decrease and a semiconductor-to-metal transition occurs. The results also show that the band gap, with applied strain on monolayer $C_2N$, can be considerably modified. These findings suggest is possible to tune the electronic properties of the $C_2N$ nanosheet by controlling the layer thicknesses, electric field and strain. We furthermore systematically investigated the effect of atom adsorption and substitution of H, O, S, F, Cl, B, C, N, Si, P, Li, Na, K, Be, Mg and Ca on $C_2N$. This leads to considerable modifications in electronic structure and the band gap of $C_2N$ can be either reduced or diminished and the system becoming a metal, half-metal, dilute-magnetic semiconductor, or semiconductor depending on the species of adatom. Moreover, the electronic and magnetic properties are significantly affected by the concentration of hydrogen and oxygen impurities and the formation of N vacancies in the holey site of monolayer $C_2N$, exhibit diverse electronic character from metal to semiconductor and inducing magnetism in some of the configurations. Our findings provide a detailed understanding of the electronic structure of $C_2N$ and how it is modified by external field (electric, strain) and by functionalization by doping and defects. This knowledge should be very useful for studies seeking to use and tailor this new material for applications in future nano devices.

## IX. ACKNOWLEDGMENTS

This work was supported by the National Research Foundation of Korea (NRF) grant funded by the Korea government(MSIT)(NRF-2017R1A2B2011989). We are thankful for comments by Meysam Baghery Tagani from department of physics in University of Guilan and Bohayra Mortazavi from Gottfried Wilhelm Leibniz Universitat Hannover, Hannover, Germany.

[1] K. S. Novoselov, A. K. Geim, S. V. Morozov, D. Jiang, Y. Zhang, S. V. Dubonos, I. V. Grigorieva, A. A. Firsov, Electric field effect in atomically thin carbon films, Sci. 306 (5696) (2004) 666-669.

[2] M. Kaukonen, A. V. Krasheninnikov, E. Kauppinen, R. M. Nieminen, Doped graphene as a material for oxygen reduction reaction in hydrogen fuel cells: A computational study, ACS Catalysis 3 (2) (2013) 159-165.

[3] I. Cabria, M. J. López, J. A. Alonso, Enhancement of hydrogen physisorption on graphene and carbon nanotubes by Li doping, J. Chem. Phys. 123 (20) (2005) 204721.

[4] Graphene-based nanomaterials for energy storage, M. Pumera, Energy Environ. Sci. 4 (2011) 668-674.

[5] I. López-Corral, E. Germán, A. Juan, M. A. Volpe, G. P. Brizuela, DFT study of hydrogen adsorption on palladium decorated graphene, J. Phys. Chem. 115 (10) (2011) 4315-4323.

[6] Y. M. Lin, C. Dimitrakopoulos, K. A. Jenkins, D. B. Farmer, H. Y. Chiu, A. Grill, Ph. Avouris, 100-GHz transistors from wafer-scale epitaxial graphene, Sci. 327 (5966) (2010) 662-662.

[7] R. Cheng, J. Bai, L. Liao, H. Zhou, Y. Chen, L. Liu, Y. C. Lin, Sh. Jiang, Y. Huang, X. Duan, High-frequency self-aligned graphene transistors with transferred gate stacks, Proceedings of the National Academy of Sciences 109 (29) (2012) 11588–11592.

[8] Y. W. Son, M. L. Cohen, S.G. Louie, Half-metallic graphene nanoribbons, Nat. 444 (2006) 347.

[9] O. V. Yazyev, M. I. Katsnelson, Magnetic correlations at graphene edges: Basis for novel spintronics devices, Phys. Rev. Lett. 100 (4) (2008) 047209.

[10] F. Schedin, A. K. Geim, S. V. Morozov, E. W. Hill, P. Blake, M. I. Katsnelson, K. S. Novoselov, Detection of individual gas molecules adsorbed on graphene, Nat. Mater. 6 (2007) 652.

[11] R. Roldan, L. Chirolli, E. Prada, J. A. Silva-Guillen, P. San-Jose, F. Guinea, Theory of 2D crystals: graphene and beyond, Chem. Soc. Rev. 46 (2017) 4387-4399.

[12] Ch. Lee, X. Wei, J. W. Kysar, J. Hone, Measurement of the elastic properties and intrinsic strength of monolayer graphene, Sci. 321 (5887) (2008) 385–388.

[13] A. K. Geim, I. V, Grigorieva, Van der waals heterostructures, Nat. 499 (2013) 419-425.

[14] A. Resta, T. Leoni, C. Barth, A. Ranguis, C. Becker, T. Bruhn, P. Vogt, G. Le Lay, Atomic structures of silicene layers grown on Ag(111): scanning tunneling microscopy

and noncontact atomic force microscopy observations, Sci. Rep. 3 (2013) 2399.

[15] J. Gao, G. Zhang, Y. W. Zhang, Exploring Ag(111) substrate for epitaxially growing monolayer stanene: A First-Principles study, Sci. Rep. 6 (2016) 29107.

[16] Y. Xu, B. Yan, H. J. Zhang, J. Wang, G. Xu, P. Tang, W. Duan, Sh. Ch. Zhang, Large-gap quantum spin hall insulators in tin films Phys. Rev. Lett. 111 (5) (2013) 136804.

[17] A. Molle, J. Goldberger, M. Houssa, Y. Xu, Sh. Ch. Zhang, D. Akinwande, Buckled two-dimensional Xene sheets, Nat. Mater. 16 (2017) 163.

[18] Q. Tang, Zh. Zhou, P. Shen, Are MXenes promising anode materials for Li ion batteries? computational studies on electronic properties and Li storage capability of $Ti_3C_2$ and $Ti_3C_2X_2$ (X = F, OH) monolayer, J. Amer. Chem. Soc. 134 (40) 16909-16916 (2012).

[19] J. Yan, Ch. E. Ren, K. Maleski, Ch. B. Hatter, B. Anasori, P. Urbankowski, A. Sarycheva, Y. Gogotsi, Flexible MXene/Graphene films for ultrafast supercapacitors with outstanding volumetric capacitance, Adv. Func. Mater. 27 (30) (2014) 1701264.

[20] W. Yangyang, E. R. Thomas, Ch. Xingzhu, L. Neng, L. Miaoqiang, D. Liming, W. Lianzhou, Nitrogen-doped $Ti_3C_2Tx$ MXene electrodes for high-performance supercapacitors, Nano Energy 38 (2017) 368 - 376.

[21] C. Berger, Zh. Song, X. Li, X. Wu, N. Brown, C. Naud, D. Mayou, T. Li, J. Hass, A. N. Marchenkov, E. H. Conrad, P. N. First, W.A. de Heer, Electronic confinement and coherence in patterned epitaxial graphene Sci. 312 (5777) (2006) 1191–1196.

[22] D. Wei, Y. Liu, Y. Wang, H. Zhang, L. Huang and G. Yu, Synthesis of N-Doped Graphene by Chemical Vapor Deposition and Its Electrical Properties, Nano Lett. 9 (5) (2009) 1752–1758.

[23] L. Dai, D. W. Chang, J. B. Baek, W. Lu, Carbon nanomaterials: Carbon nanomaterials for advanced energy conversion and storage, Small 8 (8) (2012) 1122-1122.

[24] J. Zhang, F. Zhao, Zh. Zhang, N. Chen, L. Qu, Dimension-tailored functional graphene structures for energy conversion and storage, Nanoscale 5 (2013) 3112-3126.

[25] K. Gong, F. Du, Zh. Xia, M. Durstock, L. Dai, Nitrogen-doped carbon nanotube arrays with high electrocatalytic activity for oxygen reduction, Sci. 323 (2009) 760–764.

[26] B. Mortazavi, M. Shahrokhi, M. Raeisi, X. Zhuang, L. F. C. Pereira,T. Rabczuk, Outstanding strength, optical characteristics and thermal conductivity of graphene-like $BC_3$ and $BC_6N$ semiconductors, Carbon 149 (2019) , 733-742

[27] B. Mortazavi, M. Shahrokhi, A. V. Shapeev, T. Rabczuk, X. Zhuang, Prediction of $C_7N_6$ and $C_9N_4$: stable and strong porous carbon-nitride nanosheets with attractive electronic and optical properties, J. Mater. Chem. C doi:10.1039/C9TC03513C,

[28] A. Bafekry, S. F. Shayesteh, F. M. Peeters, $C_3N$ monolayer: exploring the emerging of novel electronic and magnetic properties with adatom adsorption, functionalizations, electric field, charging and strain, J. Phys. Chem. C. 123 (2019) 12485-12499.

[29] B. Mortazavi, Ultra High Stiffness and Thermal Conductivity of Graphene Like $C_3N$, Carbon 118 (2017) 25-34.

[30] Adsorption of molecules on $C_3N$ nanosheet: A first-principles calculations, A. Bafekry, M. Ghergherehchi, S. Farjami Shayesteh, F.M. Peeters, Chem. Phys. 526 (2019) 110442.

[31] M. Makaremi, B. Mortazavi, C. V. Singh, Adsorption of Metallic, Metalloidic, and Nonmetallic Adatoms on Two-Dimensional $C_3N$, Phys. Chem. C. 121 (2017) 18575-18583.

[32] M. B. Tagani and S. I. Vishkayi, Polyaniline ($C_3N$) nanoribbons: magnetic metal, semiconductor, and half-metal, J. Appl. Phys. 124 (2018) 084304.

[33] A. Bafekry, C. Stampfl, S. Farjami Shayesteh, F. M. Peeters, Introducing Novel Electronic and Magnetic Properties in $C_3N$ Nanosheet by Defect Engineering and Atom Substitution Phys. Chem. Chem. Phys. (2019) doi:10.1039/C9CP03853A.

[34] Adsorption of alkali and alkaline-earth metal atoms on stanene: A first-principles study", Y. Kadioglu, F. Ersan, G. Gokoglu, O. U. Akturk, E. Akturk, Mater. Chem. Phys. 180 (2016) 326 - 331.

[35] F. Ersan, O. Arslanalp, G. Gokoglu, E. Akturk, Effects of silver adatoms on the electronic structure of silicene, Appl. Surf. Sci. 311 (2014) 9 - 13.

[36] A. Bafekry, C. Stampfl, S. Farjami Shayesteh, F. M. Peeters, Exploiting the Novel Electronic and Magnetic Structure of $C_3N$ via Functionalization and Conformation Adv. Elec. Mater. (2019).

[37] M. B. Tagani, Electrical and Mechanical Properties of a Fully Hydrogenated Two-Dimensional Polyaniline Sheet, Comput. Mater. Sci. 153 (2018) 126 - 133.

[38] Zh. Guizhi, L. Kun, S. Qiang, K. Yoshiyuki and J. Puru, Lithium-doped triazine-based graphitic $C_3N_4$ sheet for hydrogen storage at ambient temperature, Comput. Mater. Sci. 81 (2014) 275-279.

[39] X. Li, S. Zhang, Q. Wang, Stability and physical properties of a tri-ring based porous g-$C_4N_3$ Sheet, Phys. Chem. Chem. Phys. 15 (2013) 7142-7146.

[40] T. Hu, A. Hashmi, J. Hong, Transparent half metallic g-$C_4N_3$ nanotubes: potential multifunctional applications for spintronics and optical devices, Sci. Rep. 4 (2014) 6059.

[41] A. Hashmi, J. Hong, Metal free half metallicity in 2D system: structural and magnetic properties of g-$C_4N_3$ on BN, Sci. Rep. 4 (2014) 4374.

[42] X. Zhang, M. Zhao, A. Wang, X. Wang, A. Du, Spin-polarization and ferromagnetism of graphitic carbon nitride materials, J. Mater. Chem. C. 1 (2013) 6265-6270.

[43] Q. Guo, Q. Yang, Ch. Yi, L. Zhu, Y. Xie, Synthesis of carbon nitrides with graphite-like or onion-like lamellar structures via a solvent-free route at low temperatures, Carbon 43 (2005) 1386-1391.

[44] J. Li, Ch. Cao, J. Hao, H. Qiu, H. Xu and H. Zhu, Self-assembled one-dimensional carbon nitride architectures. Diamond and Related Mater. 15 (2006) 1593-1600 .

[45] H. Qiu, Zh. Wang, X. Sheng, First-principles prediction of an intrinsic half-metallic graphitic hydrogenated carbon nitride, Phys. Lett. A. 377 (2013) 347-350.

[46] A. Thomas, A. Fischer, F. Goettmann, M. Antonietti, J. O. Müller, R. Schlögl, J. M. Carlsson, Graphitic carbon nitride materials: variation of structure and morphology and their use as metal-free catalysts. J. Mater. Chem. 18 (2008) 4893-4908.

[47] V. Arkady, J. P. Rabe, U. Kaiser, A. I. Cooper, A. Thomas, M. J. Bojdys, G. Algara-Siller, N. Severin, S. Y. Chong, T. Björkman, R. G. Palgrave, A. Laybourn, M. Antonietti, Y. Z. Khimyak and A. V. Krasheninnikov, Triazine-based graphitic carbon nitride: a two-dimensional semiconductor, Angewandte Chemie 126 (2014) 7580-7585.

[48] Q. Zhou, M. Wu, M. Zhang, G. Xu, B. Yao, Ch. Li, G. Shi, Graphene-based electrochemical capacitors with integrated high-performance, Materials Today Energy 6 (2017)

181-188.
[49] M. Javeed, L. E. Kwang, J. Minbok, Sh. Dongbin, J. In-Yup, J. Sun-Min, Ch. Hyun-Jung, S. Jeong-Min, B. Seo-Yoon, S. So-Dam, P. Noejung, Oh Joon Hak, Sh. Hyung-Joon, B. Jong-Beom, Nitrogenated holey two-dimensional structures, Nat. Commun. 6 (2015) 6486.
[50] B. Mortazavi, O. Rahaman, T. Rabczuk and L. F. C. Pereira, Thermal Conductivity and Mechanical Properties of Nitrogenated Holey Graphene, Carbon 106 (2016) 1-8.
[51] D.W. Ma, Q. Wang, X. Yan, X. Zhang, Ch. He, D. Zhou, Y. Tang, Zh. Lu, Z. Yang, 3d transition metal embedded $C_2N$ monolayers as promising single-atom catalysts: A first-principles study, Carbon (2016) 463 - 473.
[52] Z.D. Zheng and X.C. Wang and W.B. Mi, Tunable electronic structure of monolayer semiconductor g-$C_2N$ by adsorbing transition metals: A first-principles study, Carbon 109 (2016) 764-770.
[53] Y. Song R. Yong-Chao, D. Xiang-Mei, Modulating the properties of monolayer $C_2N$: A promising metal-free photocatalyst for water splitting, Chin. Phys. B 26 (8) (2017) 087301.
[54] Z.D. Zheng and X.C. Wang and W.B. Mi, Tunable electronic structure and spin splitting in single and multiple Fe-adsorbed g-$C_2N$ with different layers: A first-principles study, J. Phys. Chem. Solid. 115 (2018) 221-227.
[55] Structural and phononic characteristics of nitrogenated holey graphene, H. Sahin, Phys. Rev. B 92 (5) (2015) 085421.
[56] S. Chakrabarty, T. Das, P. Banerjee, R. Thapa, G.P. Das, Electron doped $C_2N$ monolayer as efficient noble metal-free catalysts for CO oxidation, Appl. Surf. Sci. 418, (2017) 92 - 98.
[57] L. Zhu, Q. Xue, X. Li, T. Wu, Y. Jin, W. Xing, $C_2N$: an excellent two-dimensional monolayer membrane for He separation, J. Mater. Chem. A 3 (2015) 21351-21356.
[58] M. Guo, Y. Tan, L. Wang, Y. Hou, Diffusion of asphaltene, resin, aromatic and saturate components of asphalt on mineral aggregates surface: molecular dynamics simulation, Road Materials and Pavement Design, 18 (2017) 149-158.
[59] M. Guo, Y. Tan, J. Wei, Using Molecular Dynamics Simulation to Study Concentration Distribution of Asphalt Binder on Aggregate Surface, J. Mater. Civil Engin. 30 (5) (2018) 04018075.
[60] Adsorption of alkali and alkaline-earth metal atoms on stanene: A first-principles study", Y. Kadioglu, F. Ersan, G. Gokoglu, O. U. Akturk, E. Akturk, Mater. Chem. Phys. 180 (2016) 326 - 331.
[61] F. Ersan, O. Arslanalp, G. Gokoglu, E. Akturk, Effects of silver adatoms on the electronic structure of silicene, Appl. Surf. Sci. 311 (2014) 9 - 13.
[62] H. Zhang, X. Zhang, G. Yang, X. Zhou, Point Defect Effects on Photoelectronic Properties of the Potential Metal-Free $C_2N$ Photocatalysts: Insight from First-Principles Computations J. Phy. Chem. C 122 10 (2018) 5291-5302
[63] M. Yagmurcukardes, S. Horzum, E. Torun, F.M. Peeters, R. T. Senger, Nitrogenated phosphorated and arsenicated monolayer holey graphenes, Phys. Chem. Chem. Phys. 18 (2016) 3144-3150.
[64] A. Bafekry, M. Ghergherehchi, S. Farjami Shayesteh, Tuning the electronic and magnetic properties of antimonene nanosheets via point defects and external fields: first-principles calculations, Phys. Chem. Chem. Phys. 21 (2019) 10552-10566.
[65] X. Wang, R. Quhe, W. Cui, Y. Zhi, Y. Huang, Y. An, X. Dai, Y. Tang, W. Chen, Zh. Wu, W. Tang, Electric field effects on the electronic and optical properties in $C_2N$/Sb van der Waals heterostructure, Carbon 129 (2018) 738-744.
[66] A. Bafekry, B. Mortazavi, S. Farjami Shayesteh, Band gap and magnetism engineering in Dirac half-metallic $Na_2C$ nanosheet via layer thickness, strain and point defects, J. Mag. Magnet. Mater. 491 (2019) 165565.
[67] Y. Z. Abdullahi, T. L. Yoon, Th. L. Lim, Elastic and electronic properties of $C_2N$ monolayer: first-principles calculation, Mater. Res. Exp. 6 (2) (2019) 025601.
[68] Sh. Guan, Y. Cheng, Ch. Liu, J. Han, Y. Lu, Sh. A. Yang, Y. Yao, Effects of strain on electronic and optic properties of holey two-dimensional $C_2N$ crystals, Appl. Phys. Lett. 107 (23) (2015) 231904.
[69] H.L. Yu, X.F. Jiang, M.Q. Cai, J.F. Feng, X.S. Chen, X.F. Yang, Y.S. Liu, Electronic and magnetic properties of zigzag $C_2N$-h2D nanoribbons: Edge and width effects, Chem. Phys. Lett. 685 (2017) 363-370.
[70] J. J. He, Y. D. Guo, X. H. Yan, H. Li. Zeng, Electronic, magnetic and transport properties of transition metal-doped holely $C_2N$-h2D nanoribbons, Physica B: Condensed Matter 528, (2018) 1-8.
[71] Z.D. Zheng, X.C. Wang, W.B. Mi, Tunable electronic structure in stained two dimensional van der Waals g-$C_2N$/$XSe_2$ (X = Mo, W) heterostructures, Physica E: Low-dimensional Systems and Nanostructures 94 (2017) 148-152.
[72] R. Kumar, D. Das, A. K. Singh, $C_2N$/WS2 van der Waals type-II heterostructure as a promising water splitting photocatalyst, J. Catal. 359 (2018) 143-150
[73] M. R. A. Kishore, P. Ravindran, Tailoring the electronic band gap and band edge positions in the $C_2N$ monolayer by P and As substitution for photocatalytic water splitting, J. Phys. Chem. C 121 (40) (2017) 22216-22224.
[74] M. R. A. Kishore, A. O. Sjastad, P. Ravindran, Influence of hydrogen and halogen adsorption on the photocatalytic water splitting activity of $C_2N$ monolayer: A first-principles study, Carbon 141 (2019) 50 - 58.
[75] T. Ozaki, K. Nishio, H. Kino, Efficient implementation of the nonequilibrium Green function method for electronic transport calculations Phys. Rev. B 81 (2010) 035116 .
[76] N. Troullier, J. Martins, Efficient pseudopotentials for plane-wave calculations, Phys. Rev. B 43 (1991) 1993-2006.
[77] Variationally optimized atomic orbitals for large-scale electronic structures, T. Ozaki, Phys. Rev. B 67 (2003) 155108.
[78] T. Ozaki and H. Kino, Numerical atomic basis orbitals from H to Kr, Phys. Rev. B 69 (2004) 195113.
[79] J. P. Perdew, K. Burke and M. Ernzerhof, Generalized Gradient Approximation Made Simple, Phys. Rev. Lett. 77 (1996) 3865-3868.
[80] H. J. Monkhorst and J. D. Pack, Special points for Brillouin-zone integrations, Phys. Rev. B 13 (1976) 5188-5192.
[81] T. Bučko, J. Hafner, S. Lebègue and J. G. ngyán, Improved Description of the Structure of Molecular and Layered Crystals: Ab Initio DFT Calculations with van der Waals Corrections, J. Phys. Chem. A 114 (2010) 11814-11824.
[82] Theory and Application for the Scanning Tunneling Microscope, J. Tersoff and D. R. Hamann, Phys. Rev. Lett. 50 (1983) 1998-2001.
[83] I. Horcas, R. Fernández, J. M. Gómez-Rodríguez, J. Colchero, J. Gómez-Herrero and A. M. Baro, WSXM: A software for scanning probe microscopy and a tool for nanotechnology, Rev. Scien. Inst. 78 (2007) 013705.

[84] R. S. Mulliken, Electronic Population Analysis on LCAOMO Molecular Wave Functions. IV. Bonding and Antibonding in LCAO and ValenceBond Theories, J. Chem. Phys. 23 (1955) 2343-2346.

[85] José M Soler, E. Artacho, J. D. Gale, A. García, J. Junquera, P. Ordejón and D. Sánchez-Portal, The SIESTA method for ab initio order-N materials simulation, J. Phys.: Condensed Matter 14 (2002) 2745.

[86] Y. Qu, F. Li, H. Zhou, M. Zhao, Highly efficient quantum sieving in porous graphene-like carbon nitride for light isotopes separation Sci. Rep. 6 (2016) 19952.

[87] Xu, B. and Xiang, H. and Wei, Q. and Liu, J. Q. and Xia, Y. D. and Yin, J. and Liu, Z. G., Two-dimensional graphene-like $C_2N$: an experimentally available porous membrane for hydrogen purification, Phys. Chem. Chem. Phys. 17 (2015) 15115-15118.

[88] I. Choudhuri, B. Pathak, Ferromagnetism and half-metallicity in atomically thin holey nitrogenated graphene based systems, Chem. Phys. Chem. 18 (17) (2017) 2336-2346.

[89] R. Zhang, B. Li, J. Yang, Effects of stacking order layer number and external electric field on electronic structures of few-layer $C_2N$-h2D, Nanoscale 7 (2015) 14062-14070.

[90] F. Ersan, H. Arkin, E. Aktrk, The effect of vacancies and the substitution of p-block atoms on single-layer buckled germanium selenide, RSC Adv. 7 (2017) 37815-37822.

[91] F. Ersan, A. G. Gokçe, E. Akturk, Point defects in hexagonal germanium carbide monolayer: A first-principles calculation, Appl. Surf. Sci. 389 (2016) 1 - 6.

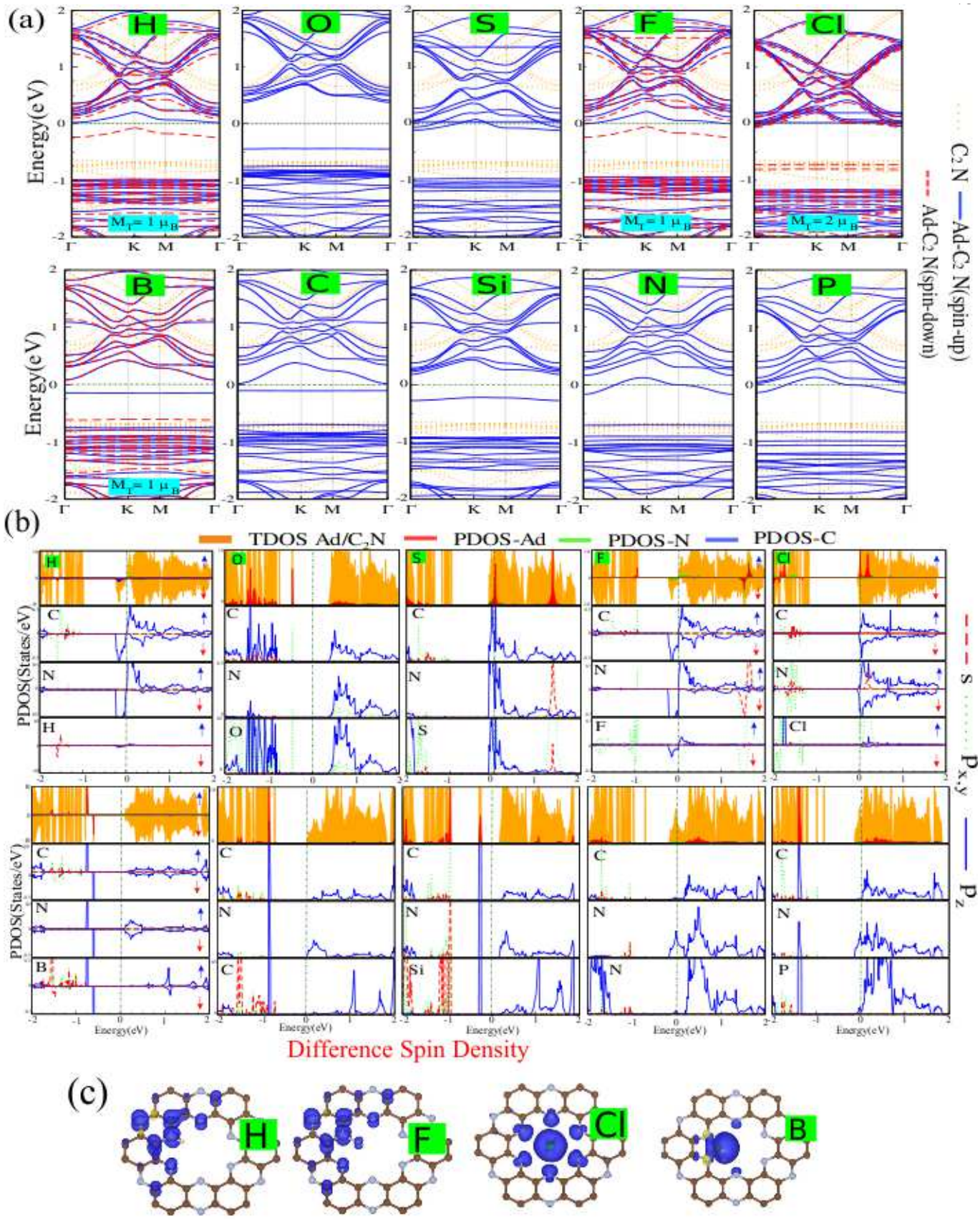


Figure 7. (a) Electronic band structure and (b) DOS and PDOS of different atoms adsorbed in the holey site of $C_2N$. The zero of energy is set at $E_F$ as shown by the dashed green-point line. (c) The difference spin density distribution. The blue and yellow colors show the ↑ and ↓ spin states, respectively.

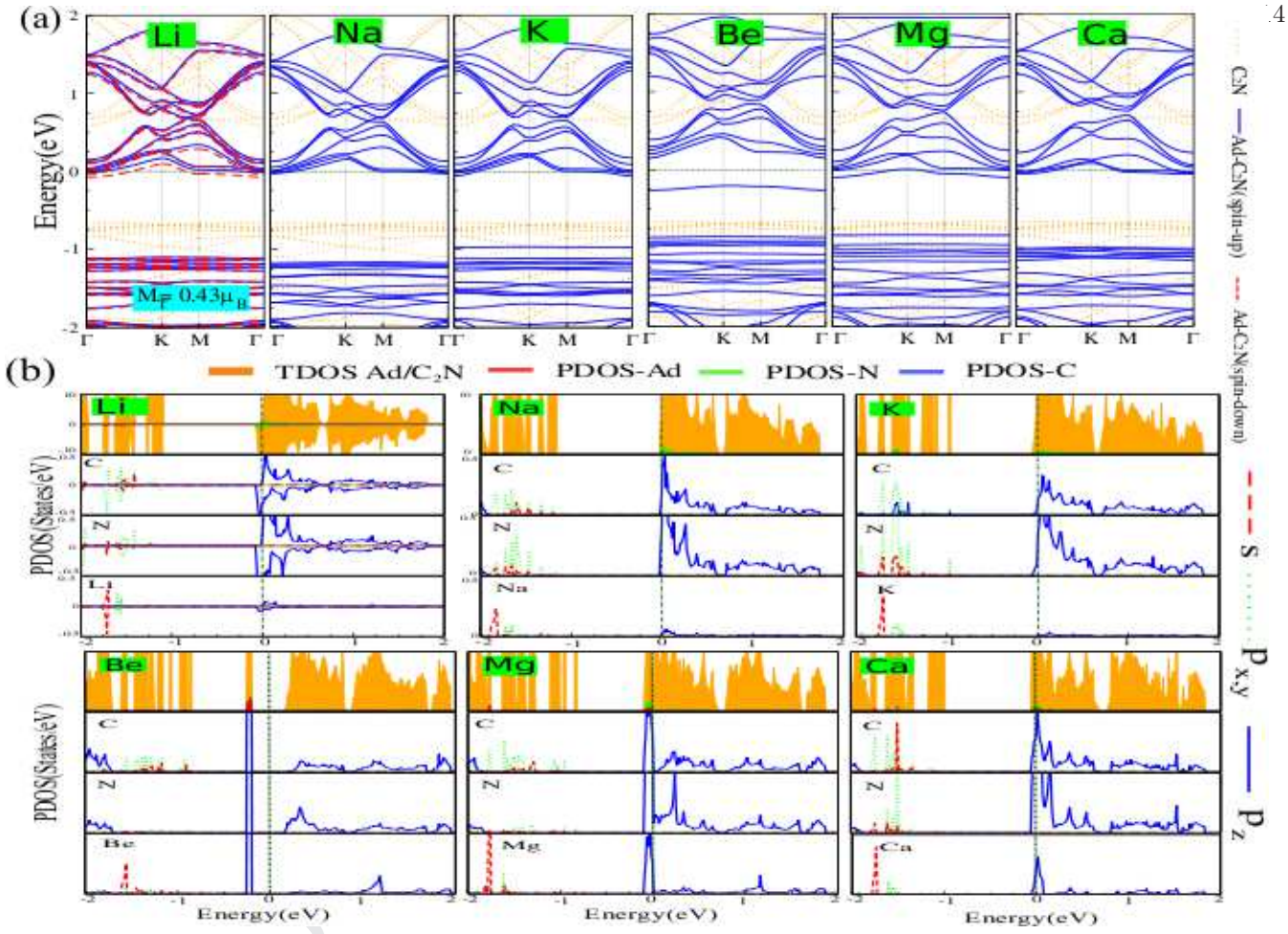


Figure 8. (a) Electronic band structure and (b) DOS and PDOS of different atoms adsorbed in the holey site of $C_2N$. The zero of energy is set at $E_F$ as shown by the dashed green-point line.

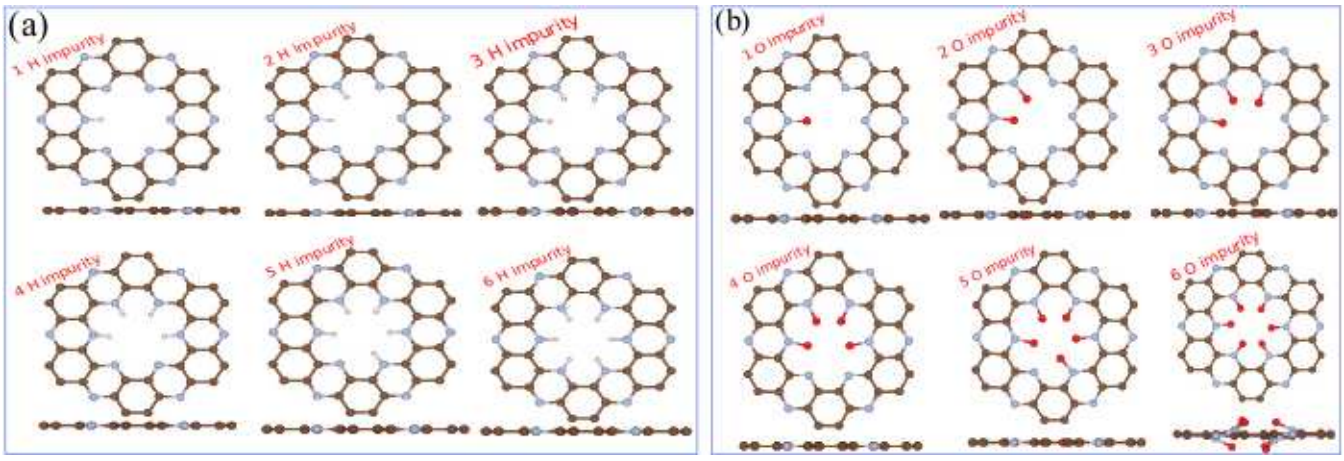


Figure 9. Optimized atomic structures of different number of impurities of (a) hydrogen and (b) oxygen atoms in the holey site of monolayer $C_2N$.

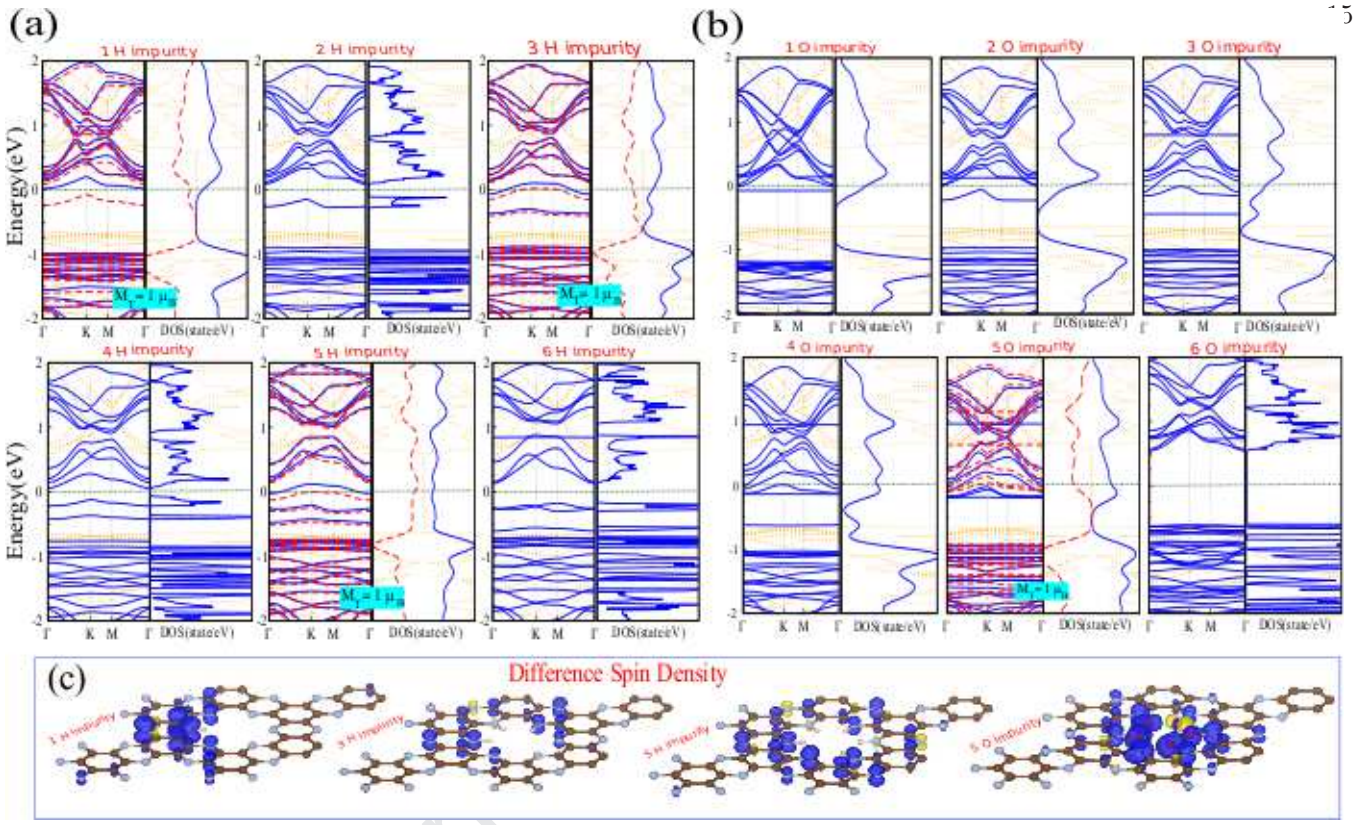


Figure 10. Electronic band structure and DOS of different number of impurities of (a) hydrogen and (b) oxygen atoms in the holey site of monolayer $C_2N$. The zero of energy is set at $E_F$ shown by the dashed green-point line. (c) The difference spin density distribution. The blue and yellow colors show the ↑ and ↓ spin states.

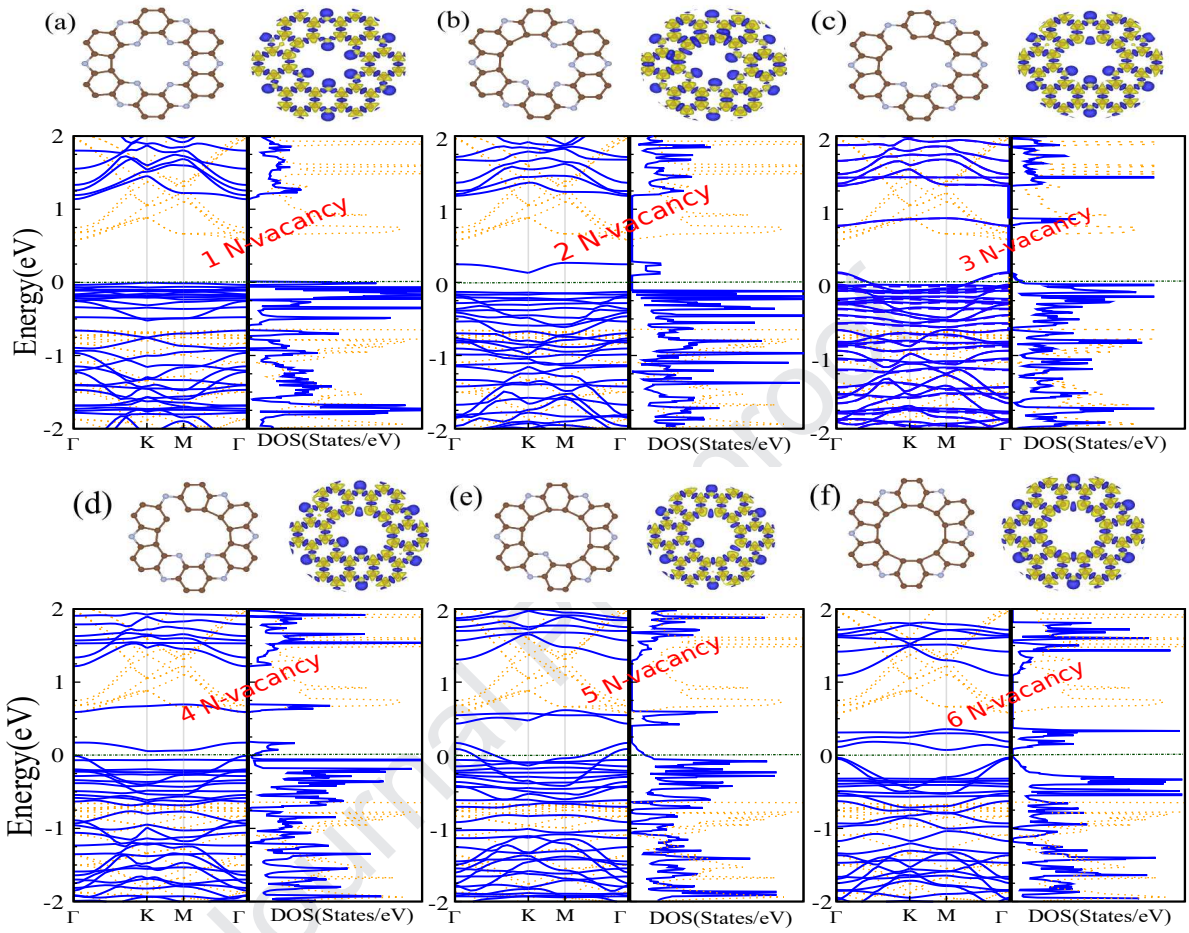


Figure 11. Optimized structures of different number of nitrogen vacancies in the holey site of $C_2N$. (a) 1N-, (b) 2N-, (c) 3N-, (d) 4N-, (e) 5N-, (f) 6N-vacancies. The difference charge density is shown in the same panel. Blue and yellow regions represent charge accumulation and depletion, respectively. The zero of energy is set at $E_F$ and shown by the dashed green-point line.

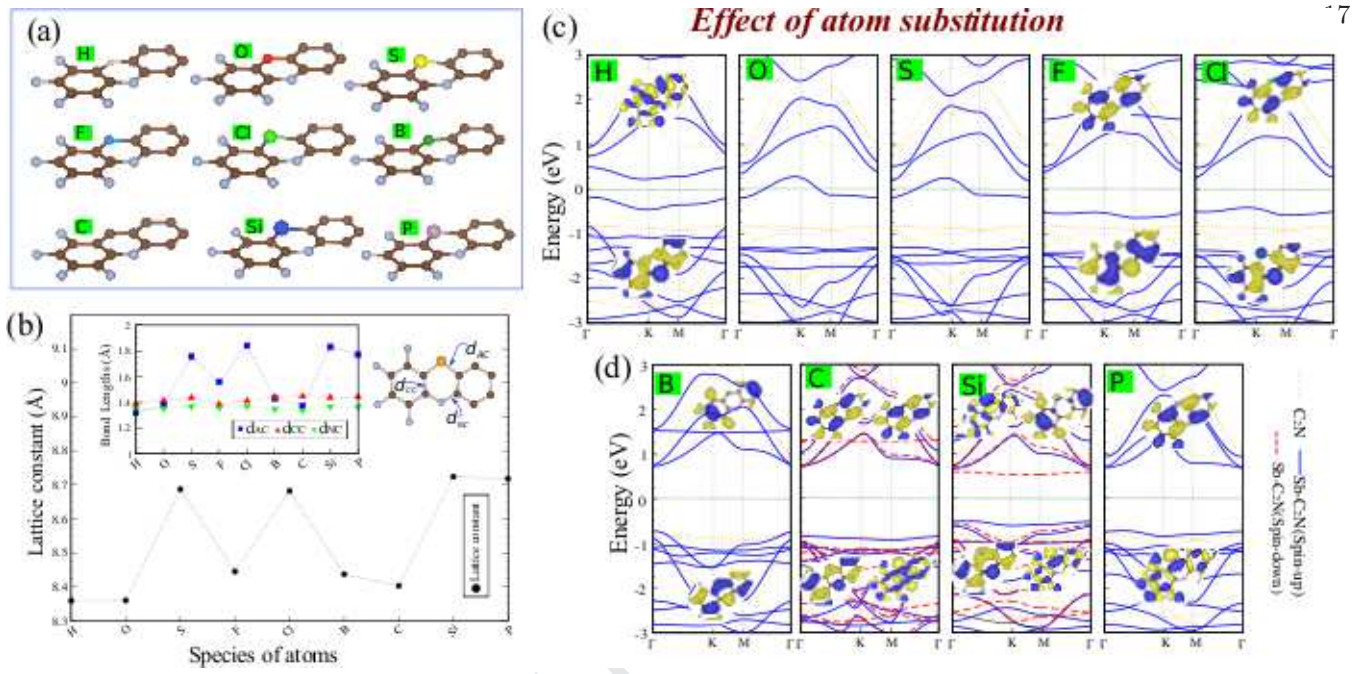


Figure 12. (a) Optimized atomic structures of H, O, S, F, Cl, B, C, Si and P atoms substituted on the N atom site of $C_2N$. (b) Structural parameters including lattice constant, atomic bond length and bond angles for different species of atoms. Schematic model view of the substitution site is indicated in the same panel. (c) Electronic band structure. VBM and CBM charge densities are indicated in the same panel. Blue and yellow regions represent the charge accumulation and depletion, respectively. The zero of energy is set at $E_F$ as shown by the dashed green-point line.

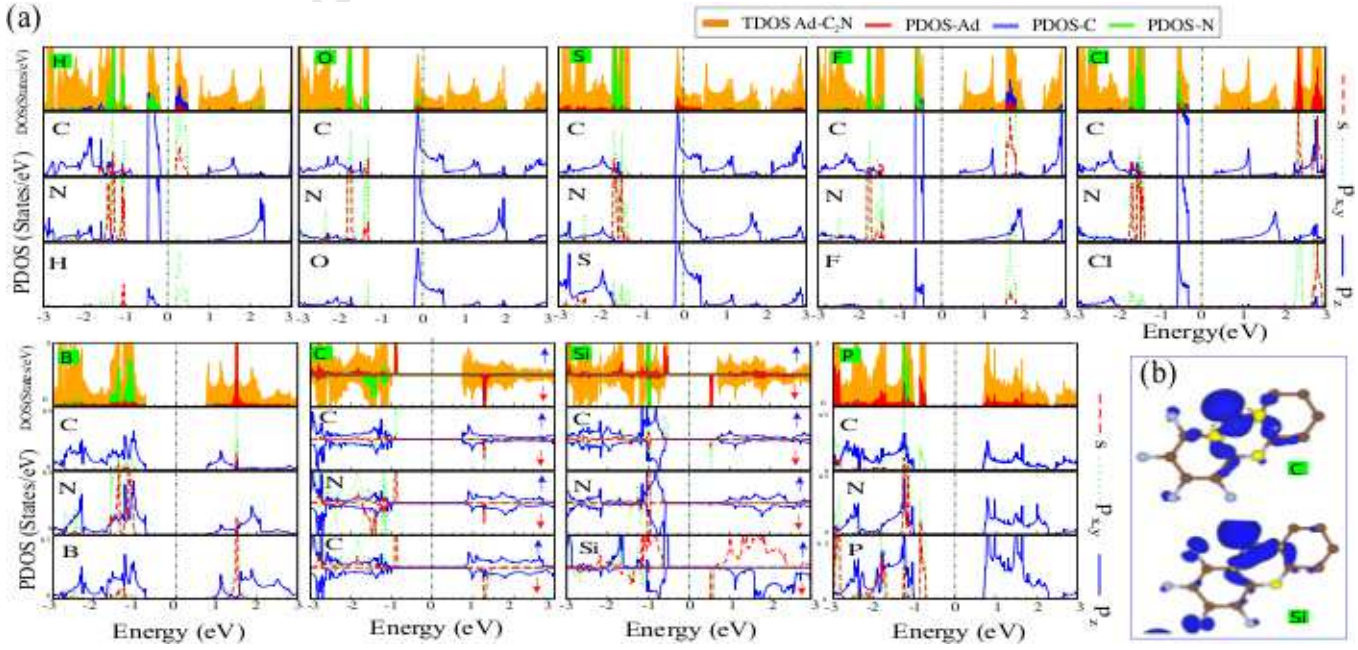


Figure 13. (a) DOS and PDOS of H, O, S, F, Cl, B, C, Si and P atoms substituted with N atom site on monolayer $C_2N$. (b) Difference spin density is shown in the inset. The blue and yellow regions represent the ↑ and ↓ spin states, respectively. The zero of energy is set at $E_F$ as shown by the dashed green-point line.

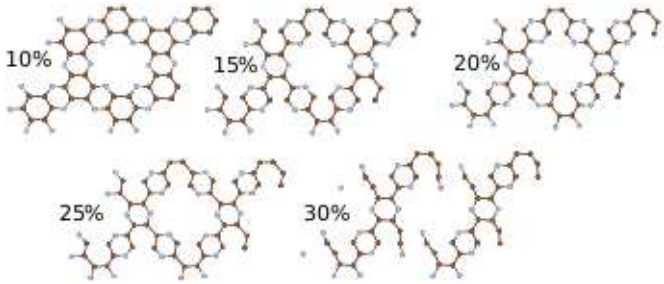


Figure 14. Optimized structures corresponding to the geometrical parameters of $C_2N$ upon the uniaxial tensile strains (along zigzag direction) 10%-30%.

I declare there are no conflicts of interest,

C. Stampfl